Nuclear Engineering and Technology 49 (2017) 1617–1628

Contents lists available at ScienceDirect

Nuclear Engineering and Technology

journal homepage: www.elsevier.com/locate/net

Original Article

# Heat transfer and flow characteristics of a cooling thimble in a molten salt reactor residual heat removal system

Zonghao Yang, Zhaoming Meng, Changqi Yan*, Kailun Chen

*Fundamental Science on Nuclear Safety and Simulation Technology Laboratory, Harbin Engineering University, 3A Laboratory Building, 145 Nantong Street, Nangang District, Harbin, Heilongjiang 150001, China*

ARTICLE INFO

*Article history:*
Received 18 January 2017
Received in revised form
21 June 2017
Accepted 21 July 2017
Available online 24 August 2017

*Keywords:*
Cooling Thimble
Flashing Flow Instability
Heat Transfer Rate
Molten Salt Reactor
Natural Circulation

ABSTRACT

In the passive residual heat removal system of a molten salt reactor, one of the residual heat removal methods is to use the thimble-type heat transfer elements of the drain salt tank to remove the residual heat of fuel salts. An experimental loop is designed and built with a single heat transfer element to analyze the heat transfer and flow characteristics. In this research, the influence of the size of a three-layer thimble-type heat transfer element on the heat transfer rate is analyzed. Two methods are used to obtain the heat transfer rate, and a difference of results between methods is approximately 5%. The gas gap width between the thimble and the bayonet has a large effect on the heat transfer rate. As the gas gap width increases from 1.0 mm to 11.0 mm, the heat transfer rate decreases from 5.2 kW to 1.6 kW. In addition, a natural circulation startup process is described in this paper. Finally, flashing natural circulation instability has been observed in this thimble-type heat transfer element.


## 1. Introduction

With today's rapid development in China, energy shortage and environmental pollution problems are becoming increasingly serious. Because of this, nuclear power has attracted more attention from society because it is clean and highly efficient. However, after the Fukushima accident, individuals worldwide maintain a vigilant and critical perspective toward the development of nuclear power, and China is no exception. Today, nuclear power is an essential energy source because of its prominent advantages. Although the pressurized water reactor is the most common type of reactor worldwide, it has potential safety risks because of its high-temperature and high-pressure boundaries. In contrast with pressurized water reactors, molten salt reactors (MSRs) have the advantages of low pressure, small size, high breeding efficiency, and little residual radioactivity [1].

The molten salt reactor concept was put forward in the early 1960s. In 1965, the Oak Ridge National Laboratory (ORNL) successfully designed and set up the MSR experiment (MSRE) [2,3], and successfully operated it for 4 years. By the end of 1969, it had fully demonstrated the feasibility of using molten fuel and a molten heat transfer medium [4]. Research into MSRs was set aside in 1972, and since then the United States has focused on the liquid metal fast breeder reactor. Japan studied the FUJI series of MSRs beginning in the 1980s, and that study is continuing today.

Beginning in the 21st century, MSR studies have gradually made their way back into the international agenda, and MSR has been proposed as the generation IV nuclear reactor. The United States proposes the fluoride salt-cooled high-temperature reactor (FHR), which has many things in common with an MSR. The FHRs use solid nuclear fuel, cooled with low-pressure molten fluoride. The goal of FHRs is to reliably and economically generate large amounts of electric power and high-temperature process heat [5]. After the Fukushima accident, Japan accelerated the pace of research process on the FUJI series of MSRs. FUJI is a thermal reactor that uses the fuel FLiBe mixed with U/Pu/Tu. The moderator is graphite, which does not need changing during the reactor core's lifetime [6]. To achieve the efficient transmutation of the transuranium elements in light water reactor spent fuel, Russia proposed to use transuranium elements instead of the U–Pu circle as a nuclear fuel to build a molten salt actinide recycler and transmuter (MOSART) [7]. France is developing a molten salt fast reactor, in which the fuel circle uses two launching modes, the $^{233}$U launch and the transuranium elements launch [8]. The technological and experimental studies of both MOSART and molten salt fast reactor have goals of

* Corresponding authors.
*E-mail addresses:* hurricane93@hrbeu.edu.cn (Z. Yang), Changqi_yan@163.com (C. Yan).

http://dx.doi.org/10.1016/j.net.2017.07.026

decreasing the generation of highly toxic radioactive waste while simultaneously generating electric power. China is also putting effort into an MSR. The Shanghai Institute of Applied Physics and Chinese Academy of Sciences plans to build a 100-MW thorium MSR by 2030.

The residual heat removal system is an important component of an MSR [9,10]. After the MSR shuts down, the fuel salt is drained into the drain salt tank through a frozen valve. Two primary plans exist to cool the fuel salt in the drain salt tank: external cooling of the drain salt tank and internal cooling using heat transfer elements. The representative method for the external cooling plan is reactor external vessel cooling (REVC), which is a mitigation strategy for a severe accident. For a reactor core meltdown, the decay heat of melt can be removed from the bottom head by two-phase natural circulation in the REVC channel; in this way, in-vessel retention is realized. Currently, this cooling method has been applied practically in the AP1000 and APR1400 [11].

For the external cooling plan design for the MSR, in reference to the REVC method of the AP1000, the drain salt tank is placed in the pool and the heat is removed by natural convection of the water outside the drain salt tank. However, if this method is used, the fuel salt at the center of the drain salt tank may not be sufficiently cooled because of the tank's very large volume, and the continuous generation of decay heat may make the temperature of the molten salt rise to a level greater than the fuel salt temperature limit. The drain salt tank is also equipped with a heater to prevent the fuel salt from solidifying during the heat removal process. When the heater runs, the pool-type residual heat removal system remains in operation, working against the efforts to maintain the molten salt temperature. Another disadvantage is that the heat dissipation power can be difficult to control.

There are several plans for internal cooling, one of which is to use a thimble-type heat transfer element designed by ORNL, which was successfully operated for 4 years. There have also been several new designs for the residual heat removal systems in recent years. One such design, developed by Wang et al. [12], immerses the drain salt tank in a secondary coolant molten salt pool, and sodium–potassium alloy (NaK) heat pipes are placed across the drain salt tank to transfer the heat from the fuel salt in the drain salt tank to the secondary coolant molten salt. Another design, developed by Ishiguro et al. [6], consists of a drain tank, a closed water circuit, and an air cooler. Heat transfer pipes with a diameter of 30 cm pass vertically through the drain salt tank. The water in the heat transfer element goes through the drain salt tank and transfers heat to the air cooler. At the outlet of the air cooler, the collected cooling water circulates back to the drain salt tank [6]. In the current study, we use a furnace to simulate the high temperature environment of molten salt. The design of Wang et al. [12] is relatively complicated, containing fuel salt and NaK liquid alloy. The dimensions of the heat transfer element designed by Ishiguro et al. [6] are relatively large, which makes furnace design challenging. Furthermore, both the designs of Wang et al. [12] and Ishiguro et al. [6] are purely theoretical. By contrast, the ORNL design has been operated successfully for 4 years, which fully proves the feasibility of a thimble-type heat transfer element. Therefore, in the current research, the experimental heat removal loop is based on the ORNL design. In the ORNL residual heat removal system, the cooling thimbles are directly inserted into the drain salt tank to remove the sensible heat and decay heat of the fuel salt. A schematic diagram of the residual heat removal system designed by ORNL is shown in Fig. 1. From the figure, it is evident that this type of residual heat removal system is not passive. If the entire system loses electricity, the water pump will shut down, and the heat of the high temperature water in the condenser cannot be removed, resulting in failure of the residual heat removal system.

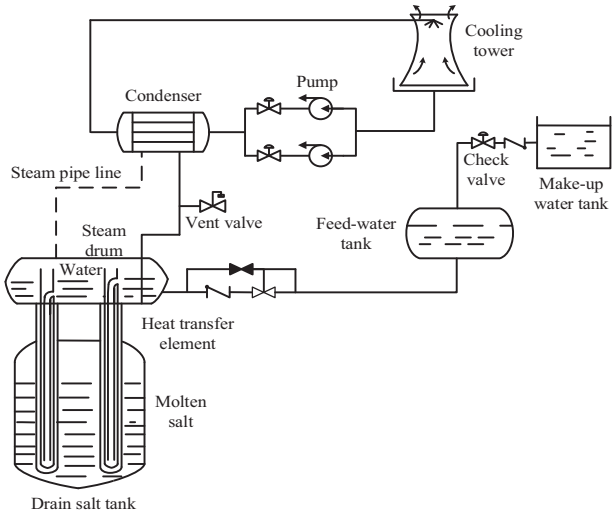


**Fig. 1.** Schematic of the MSR residual heat removal system. MSR, molten salt reactor.

Natural circulation instability is an important factor that affects the performance of natural circulation loops. The instability phenomena vary in different experimental natural circulation loops owing to variation in experimental structures, including the pipe diameter, the height of the experimental loop, the system pressure, and the heat flux [13,14]. The major flow instability phenomena observed by scholars include density wave oscillations, flashing instability, and geysering instability. Prasad et al. [15] conducted experiments under both forced and natural circulation conditions to study density wave oscillations, classifying them into two types. Type I instability is a low frequency oscillation that occurs at low pressure and low mass flow rate. This type of instability is dominated by gravity effects in the unheated riser section; the hydrostatic head is very sensitive to flow rate fluctuations. Type II instability, occurring at high power and low inlet subcooling, is attributable to the interaction between the mass flux, two-phase flow pressure loss, and void formation. Flashing instability often occurs when the structure of the experimental loop is high, and both system pressure and heating power are low, which implies large saturation temperature differences between the inlet and the outlet of the rising section. At low heating power, the coolant may not reach saturation conditions in the heating section. However, because of the strong variation of saturation temperature across the system, flashing can occur in the rising section [16,17]. Furuya et al. [18] regard flashing instability as a type of density wave instability [18]. However, Tanimoto et al. [19] and Shi et al. [20] consider that flashing instability has its own characteristics that are different from other instabilities. Geysering instability occurs for a certain range of inlet subcooling temperatures [21,22]. In general, the driving force is insufficient and the main stream flows slowly or is stagnant. Additionally, the slug developed from the heating section will be condensed into water in the rising section. Duffey and Rohatgi [23] divided the geysering into three phases: oscillation, venting, and reflux. Jiang et al. [16] investigated the geysering phenomenon in detail and found that the mass flow rate oscillates with high peak values such as pulses without a regular period. The energy released by the pressure wave resulting from the condensation of subcooled vapor causes strong mechanical vibrations in the system [16].

In the current research, an experimental natural circulation loop is designed and built with a single cooling thimble by reference to the design of ORNL. The heat transfer and flow characteristics are analyzed for the MSR cooling thimble. The influence of the cooling thimble gas gap width on heat transfer is analyzed using

experimental results and calculation results. The phenomenon of the experimental startup process is analyzed, and the flashing natural circulation instability is observed and analyzed in this natural circulation system. To some extent, the results provide references to the design of the cooling thimble and the heat removal of molten salt in the drain salt tank.

## 2. Experimental natural circulation loop

An experimental natural circulation loop is designed and built to simulate the heat transfer process in the passive residual heat removal system of an MSR. The experimental loop is designed with a single cooling thimble based on the ORNL design. A schematic layout of the test loop is shown in Fig. 2. This experimental loop removes the redundant part of ORNL's design, and the new, compact design can remove residual heat passively. The entire system consists of two natural circulation loops, one of which is the heat transfer element itself. The other natural circulation loop is the steam dome and the pipeline between the steam dome and the condenser.

In this experiment, a high-temperature electric furnace is used to simulate the high-temperature environment of the molten salt. The heat transfer element consists of three concentric pipes. There is a thimble outside the bayonet. Without the thimble, there would be a very large temperature difference and consequently high thermal stress on the bayonet, which is located between the coolant water and the high temperature molten salt. This structure can effectively avoid accidents (such as an explosion) that can occur when there is only a single thimble, which can be damaged by corrosion when high-temperature molten salt touches the coolant water directly. The structure of the heat transfer element and the thermocouple arrangements are shown in Fig. 3. The dimensions of the cooling thimble in both this experimental loop and the ORNL MSR are shown in Table 1. In the heat transfer element of the natural circulation loop, the water coolant flows down through the feed tube (downward channel). When it reaches the bottom, it will turn and flow upward through the rising channel because of the heat from the thimble. The driving force of the system depends on the density difference between the downward channel and the rising channel. The water in the cooling thimble absorbs heat and generates steam. The steam then passes through the steam dome and flows into the condenser, where it is condensed and then flows back to the steam dome. The previous steps describe the primary heat removal process in this experiment.

Prior to the experiment, the water in the steam dome and condenser is heated to boiling. Next, the noncondensable gas in the experimental loop is drained out. The experiment will not begin until the water temperature in the condenser and the system pressure stabilize. The steam flow rate is measured indirectly by measuring the amount of condensed water. When the system stabilizes, the ball valve, located below the glass tube, will be shut. The steam generated from the heat transfer element is condensed into water in the condenser. The condensed water is then received in the glass tube and the liquid level variation is recorded over time.

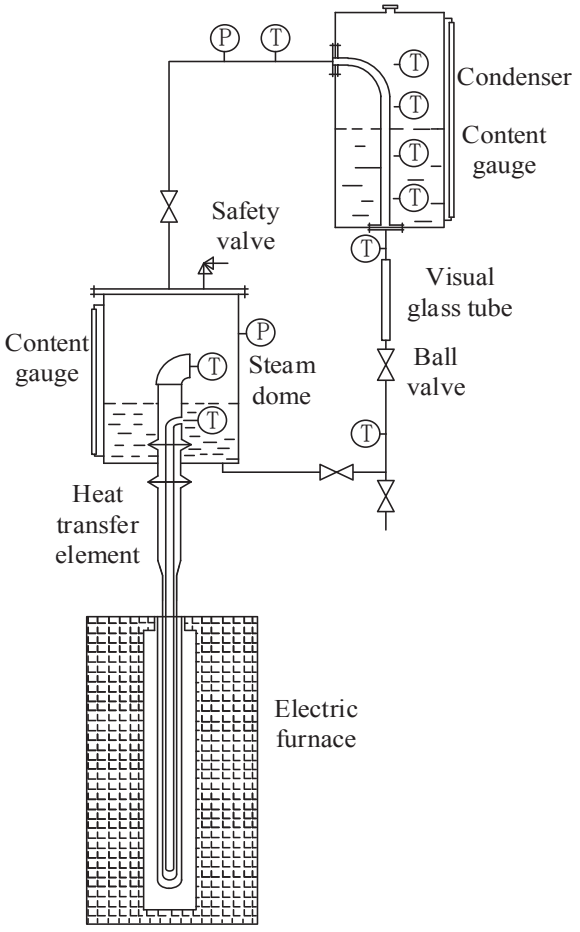


**Fig. 2.** Schematic of the test loop. P, pressure transmitter; T, thermocouple.

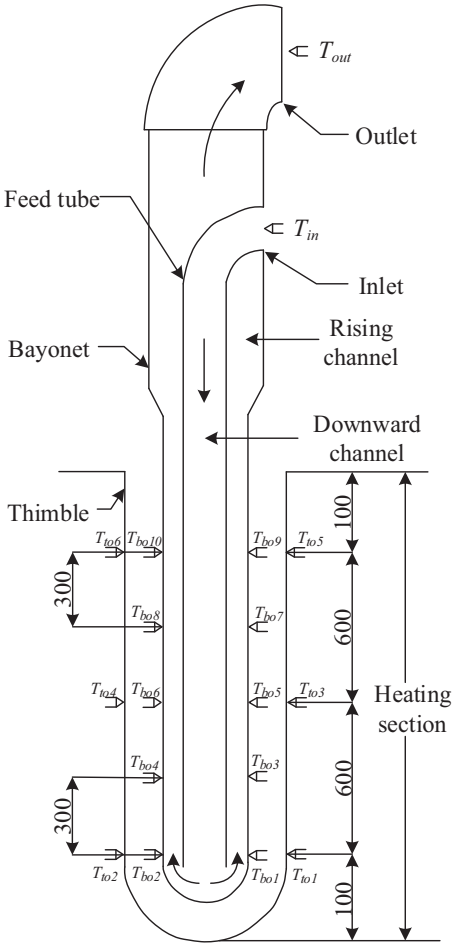


**Fig. 3.** Schematic layout of the cooling thimble with thermocouple locations. $T_{bo}$, bayonat outer wall temperature; $T_{to}$, thimble outer wall temperature; $T_{in}$, inlet temperature, $T_{out}$, outlet temperature; The unit of the numbers used in the figure is millimeter.

**Table 1**
Original dimensions of the heat transfer element.

| Structure | | Dimensions |
|---|---|---|
| Cooling thimble | Feed tube | 12.70 mm × 1.19 mm, 2.97 m in length |
| | Bayonet | 25.60 mm × 1.5 mm, 3.10 m in length |
| | Thimbles (a), (b), (c) | 31.88 mm × 1.15 mm, 38.08 mm × 1.18 mm, 45.16 mm × 1.47 mm, 1.395 m in length |
| | Heating section | 1.395 m |
| Cooling thimble designed by ORNL [24] | Feed tube | 12.70 mm (0.5 inch), 1.994 m and 2.096 m in length |
| | Bayonet | 25.40 mm (1 inch), 2.149 m in length |
| | Thimble | 38.10 mm (1.5 inch), 1.968 m in length |
| | Heating section | 1.689 m |

ORNL, Oak Ridge National Laboratory.

For better accuracy of the temperature measurements, the pipe wall is grooved with keyways along its axial direction. A photograph of a keyway and a soldered dot is shown in Fig. 4A. The dimensions of the keyways are 5 cm (length), 2 mm (width), and 0.5 mm (depth); the sheathed K-type thermocouples are buried into the keyways by silver brazing. This method is effective at avoiding the phenomenon in which the measured wall temperature is slightly higher than the true wall temperature because of the radial temperature gradient in the furnace chamber. As shown in Fig. 4B, in the method of traditional electric fusion welding, the thermocouples are welded on the pipe wall in the radial direction. Even when the welding is done correctly, there will be approximately 1 mm of the thermocouple that is perpendicular to the pipe wall. When the furnace temperature is 700°C, there will be about a 500°C temperature difference in the air layer between the thimble and the bayonet. The air temperature near position X will be slightly higher than that near position Y. However, the temperature of the thermocouple wire at position X will be similar to the temperature of the soldered point at position Y, and the thermocouple measurement of the soldered point that is simply welded on the pipe wall will be higher than the temperature of air near the soldered point. The reason for this phenomenon is that the thermocouple wire at position X, because of the low thermal resistance of thermocouple, prefers to transfer heat to the soldered point at position B through the thermocouple itself rather than through the air. Location pins welded on the pipe wall are used to keep the pipes concentric.

## 3. Calculating the heat transfer and flow

In addition to the experimental loop, a self-compiling program was developed to study the change in cooling thimble heat transfer rate with specific detailed pipe diameters. The locations of the wall temperature measurements, and the pipe diameters, are shown in Fig. 5. The simplified calculation processes for the heat transfer rate and mass flow rate are shown in Fig. 6. A thermal resistance schematic of the cooling thimble is shown in Fig. 7. For the calculation of the heat transfer and flow processes, first, assume an initial heat transfer rate $\Phi_1$ and an initial superheat $\Delta T_{sat,1}$ of the feed tube inner wall. The heat transfer rate $\Phi_2$ and superheat $\Delta T_{sat,2}$ are obtained through the series of calculations shown in the figure. It is necessary to note that $\Phi_1$ and $\Delta T_{sat,1}$ are the initial assumption values, $\Phi_2$, $\Delta T_{sat,2}$, and the others are the iterative values during the iteration process. The specific calculation equations for $\Phi$ are shown in Eqs. (12–14). $\Phi_1$ and $\Delta T_{sat,1}$ will be changed until $\Phi_1$ is equal to $\Phi_2$ and $\Delta T_{sat,1}$ is equal to $\Delta T_{sat,2}$. Assume an initial mass flow rate $M$. By doing so, the two-phase flow pressure drop will be obtained. Then, the initial $M$ will be revised until the sum of the four types of pressure drop is equal to the driving pressure head $P_d$. Finally, the heat transfer processes and the flow processes are coupled to obtain the final heat transfer rate and mass flow rate.

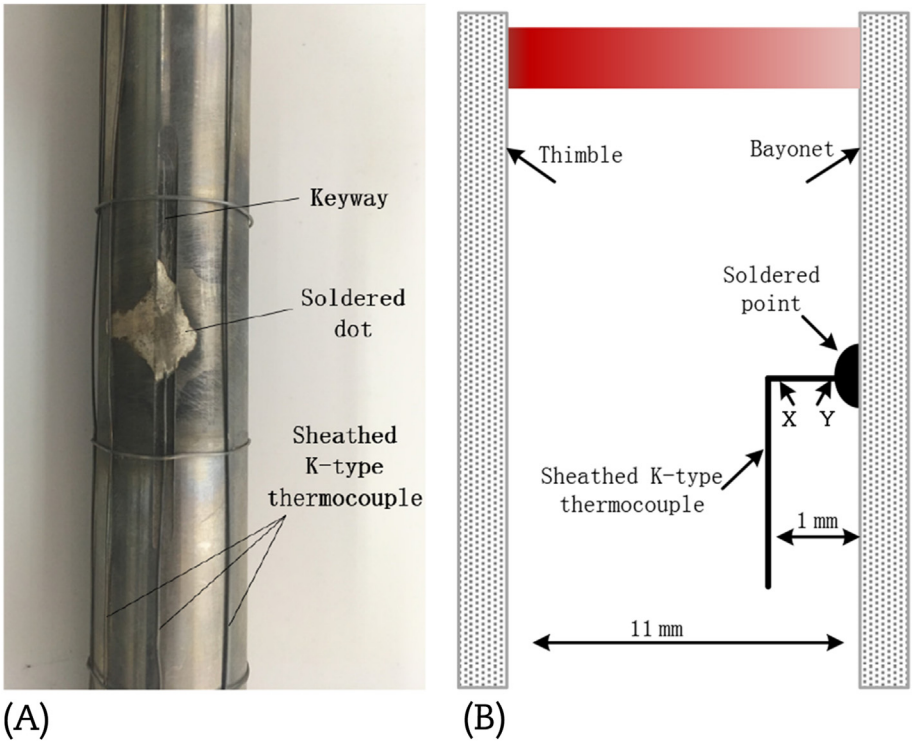


**Fig. 4.** Photograph and schematic of welding methods. (A) Method used in the experiment. (B) Traditional method. X, thermocouple location slightly far from the soldered point; Y, thermocouple location close to the soldered point.

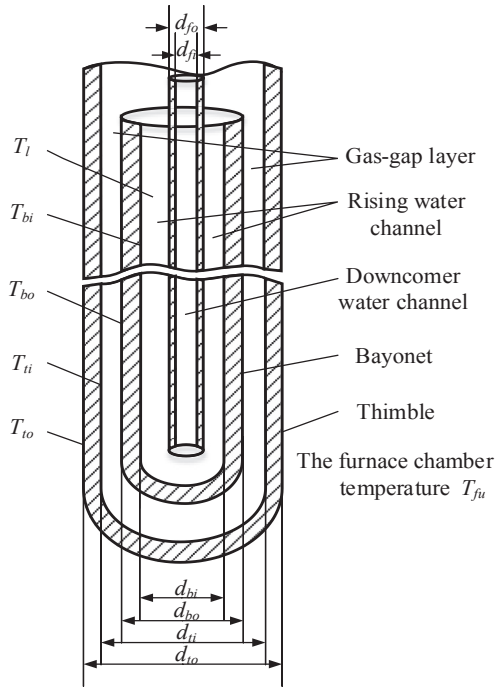


**Fig. 5.** Locations of wall temperature measurements and pipe diameter. $T_l$, liquid temperature; $T_{bi}$, bayonet inner wall temperature; $T_{bo}$, bayonet outer wall temperature; $T_{ti}$, thimble inner wall temperature; $T_{to}$, thimble outer wall temperature; $T_{fu}$, furnace temperature; $d_{bi}$, bayonet inner wall diameter; $d_{bo}$, bayonet outer wall diameter; $d_{ti}$, thimble inner wall diameter; $d_{to}$, thimble outerwall diameter.

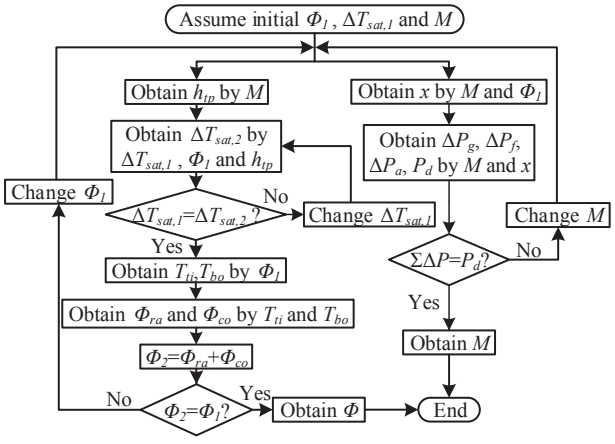


**Fig. 6.** Calculation process for heat transfer rate and mass flow rate. $\Phi$, heat transfer rate; $T_{bi}$, bayonet inner wall temperature; $T_{bo}$, bayonet outer wall temperature, $T_{sat}$, saturation water temperature; $\Delta T_{sat}$, $T_{bi}$-$T_{sat}$, inner wall superheat of thimble; $M$, Mass flow rate; $h_{tp}$, two-phase heat transfer coefficient; $\Phi_{co}$, conduction heat transfer rate; $\Phi_{ra}$, radiation heat transfer rate, x, dryness fraction; $\Delta P_g$, gravity pressure drop; $\Delta P_a$, acceleration pressure drop; $\Delta P_f$, friction pressure drop; $P_d$, driving force pressure.

To calculate the heat transfer coefficient, the classical Chen formula [25] is applied for saturated and subcooled flow boiling. The Chen formula is listed as follows:

$$h_{tp} = h_{pool} \cdot S + h' \cdot F \tag{1}$$

$$h_{pool} = 0.00122 \cdot \left( \frac{(k')^{0.79} C_p^{0.45} (\upsilon'')^{0.24}}{\sigma^{0.5} (\mu')^{0.29} (H'' - H')^{0.24} (\upsilon')^{0.49}} \right) \Delta T_{sat}^{0.24} \Delta P_{sat}^{0.75} \tag{2}$$

$$h' = 0.023 \cdot (Re')^{0.8} (Pr')^{0.4} \left( \frac{k'}{D_{rc}} \right) \tag{3}$$

$$S = \left( 1 + 2.53 \cdot 10^{-6} (Re')^{1.17} \right)^{-1} \tag{4}$$

$$F = 2.53 \cdot (1/X_{tt} + 0.213)^{0.736} \tag{5}$$

$$F = 1, \tag{6}$$

where $h_{pool}$ is the pool boiling heat transfer coefficient and $h'$ is the liquid phase convective heat transfer coefficient. The parameter $S$ is the suppression factor and accounts for the fact that the pool boiling correlations overpredict the actual nucleate boiling. The parameter $F$ is called the enhancement factor and accounts for the enhancement of forced convection heat transfer because of the existence of vapor. For subcooled flow boiling, the effect of the gas phase is negligible compared to that in saturation boiling. Eq. (5) is then rewritten as Eq. (6) [26].

To calculate the two-phase flow pressure drop, a homogeneous flow model is used. Several assumptions are made for the calculation. First, in the rising channel, the vapor and liquid have equal linear velocities. Second, thermodynamic equilibrium is attained between the vapor and liquid phases. Third, the two-phase friction factor $fr_{tp}$ is assumed to be equal to that which would have occurred had the total flow been assumed to be all liquid. And the friction factor $fr_{tp}$ is evaluated using a mean two-phase viscosity $\mu_{tp}$ in the normal friction factor relationships [27]. Additionally, the thimbles are considered to be heated uniformly in the axis direction. The primary calculation equations are given by Eqs. (7–11). The friction pressure drop through the nonheating section and the pressure drops through the enlargement and bend are not listed in there, because the formula of them are similar to $\Delta P_f$, $\Delta P_g$, and $\Delta P_a$.

$$\Delta P_f = \frac{2 \cdot fr_{tp} G_{rc}^2 L_{ba} \upsilon'}{D_{rc}} \left[ 1 + \frac{x}{2} \left( \frac{\upsilon'' - \upsilon'}{\upsilon'} \right) \right] \tag{7}$$

$$fr_{tp} = 0.079 \cdot \left( G_{rc} D_{rc} / \mu_{tp} \right)^{-0.25} \tag{8}$$

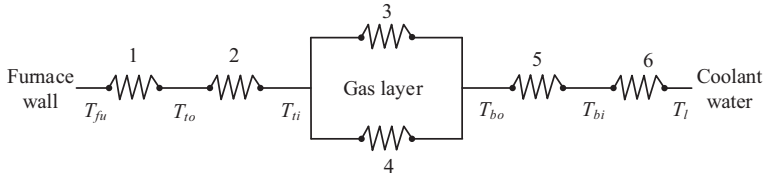


1, Conduction and radiationthermal resistance; 2, Thimble thermal resistance; 3, Radiation thermal resistance; 4, Conduction thermal resistance; 5, Bayonet thermal resistance; 6, Convectionthermal resistance

**Fig. 7.** Thermal resistance schematic for the cooling thimble. $T_{fu}$, furnace temperature; $T_{to}$, thimble outer wall temperature; $T_{ti}$, thimble inner wall temperature; $T_{bo}$, bayonet outer wall tempearture; $T_{bi}$, bayonet inner wall temperature; $T_l$, liquid temperature.

$$\frac{1}{\mu_{tp}} = \frac{x}{\mu''} + \frac{1-x}{\mu'} \tag{9}$$

$$\Delta P_g = \frac{gL_{ba}}{(\upsilon'' - \upsilon')x} \ln\left[1 + x\frac{\upsilon'' - \upsilon'}{\upsilon'}\right] \tag{10}$$

$$\Delta P_a = G_{rc}^2 \cdot \left(\upsilon'' - \upsilon'\right) \cdot x \tag{11}$$

## 4. Analysis of heat transfer and flow characteristics near the cooling thimble

### 4.1. Startup process for the experimental natural circulation loop

Before the experiment, the noncondensed air in the system should be drained out. The change in the steam dome pressure with time is shown in Fig. 8. The steam dome pressure is simplified as $P_{sd}$.

As shown in Fig. 8, $P_{sd}$ increases slowly during the first 400 s. Little vapor is generated from the heat transfer element because of the large subcooling of water. As time passes, the speed of vapor generation accelerates, resulting in the rapid increase in $P_{sd}$. In Fig. 8, arrow A corresponds to the stage at which $P_{sd}$ starts to fluctuate and ceases to rise. When $P_{sd}$ reaches the pressure limit of the safety relief valve installed on the steam dome, the valve opens automatically and the mixture of vapor and noncondensed air is drained out. The valve closes automatically when the pressure decreases below the pressure limit. This process lasts approximately 500 s, during which the valve opens and closes several times. $P_{sd}$ decreases when the share of noncondensed air decreases to a certain limit, at which point the vapor can be condensed effectively by the condenser without the hindrance of noncondensed air. Next, $P_{sd}$ decreases to a stable state at which the heat brought in by the furnace is equal to the heat taken away by the condenser. Over time, the temperature of the water in the condenser continues to increase. With the decrease in the temperature difference between the inside and outside of the condenser tube, the heat transfer efficiency decreases. However, there is continuous vapor generated from the steam dome. Thus, $P_{sd}$ increases after 8000 s. Stage B's phenomenon occurs when the water in the condenser changes from subcooled boiling to saturation boiling. The heat transfer efficiency is enhanced, so $P_{sd}$ decreases for a short time. In the end, the system reaches a stable state and $P_{sd}$ stops changing. The previous discussion describes the startup process of the natural circulation experiment.

### 4.2. Flashing natural circulation instability

In this experiment, the flow rate is not measured because of the structure specificity of the cooling thimble. In the cooling thimble, the downward channel is filled with a single-phase liquid, but it is surrounded by the rising channel where the boiling occurs. Because the flowmeter cannot be installed in the boiling loop, only the temperature and $P_{sd}$ are analyzed during the flow instability process.

There are two aspects that affect the water boiling in this experiment. First, there is flow boiling when the water passes through the headed thimble that is heated. Second, there is flashing boiling in the rising channel. As shown in Figs. 9A and 9B, at a $T_{fu}$ of 700°C, the inlet and outlet temperatures of the cooling thimble fluctuate periodically. However, when $T_{fu}$ reaches 800°C, the fluctuation disappears. Moreover, there is only a small temperature difference between the cooling thimble inlet and outlet (the outlet temperature is approximately 1°C higher than the inlet temperature). Because of this, we can discover that the flow boiling phenomenon has always been there. However, at a $T_{fu}$ of 700°C, the flow boiling intensity is not strong enough. The small amount of vapor results in a low natural circulation driving force, which causes a low flow rate. The slow movement of the main stream cannot remove enough heat from the furnace, resulting in a gradual increase in wall temperature. Finally, the flashing instability phenomenon is introduced. However, when $T_{fu}$ is 800°C, there is a very small amount of fluctuation, which demonstrates that flow boiling plays a major role at this temperature.

From the viewpoint of the fluctuation period, the flashing appears about every 50s; in each period, we find that energy is accumulated and released. The fluctuation amplitude of the upper heating section is a little larger, approximately 10°C, and the fluctuation amplitude of the lower heating section is a little smaller, approximately 5°C. On the whole, the fluctuation is relatively obvious, and the influence on the wall temperature fluctuation is not restricted to the growth and separation of bubbles on the pipe wall. In theory, the flashing will appear only when the temperature of the main stream reaches a certain point. In this experiment, the inlet water temperature is close to saturation temperature, a characteristic that other kind types of flow instability do not share. Synthesizing the above analyses, we conclude that the observed kind of flow instability phenomenon is flashing flow instability.

Fig. 9 shows the periodic variation of the wall temperature and $P_{sd}$ with time at $T_{fu} = 700$°C. An IMP3595A data acquisition is used to collect the data, using a collection frequency of 1 second. In Fig. 9, the time interval between two adjacent points is 1 second. As shown in Fig. 9, four different stages (A to D) of wall temperature variation during a flashing period are marked out with arrows. At the beginning, $T_{bo}$ increases slowly with time, and after reaching a

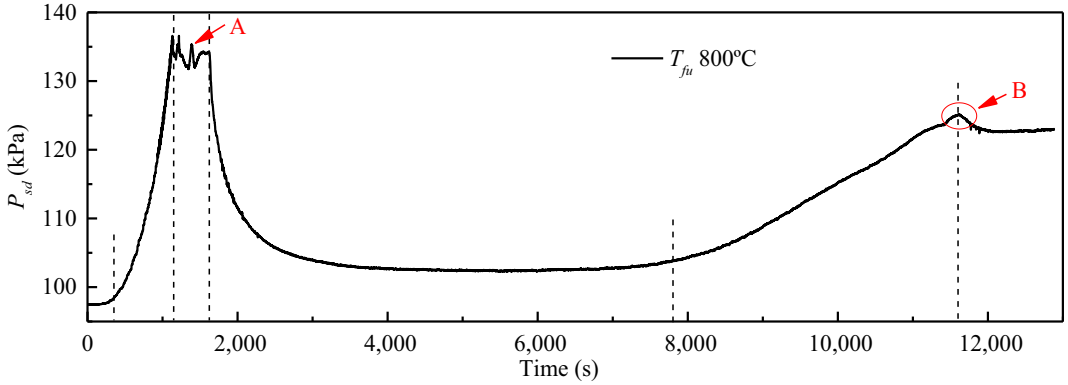


**Fig. 8.** Change of $P_{sd}$ with time. $P_{sd}$, steam dome pressure; $T_{fu}$, furnace temperature; A, pressure fluctuation stage; B, saturation boiling stage.

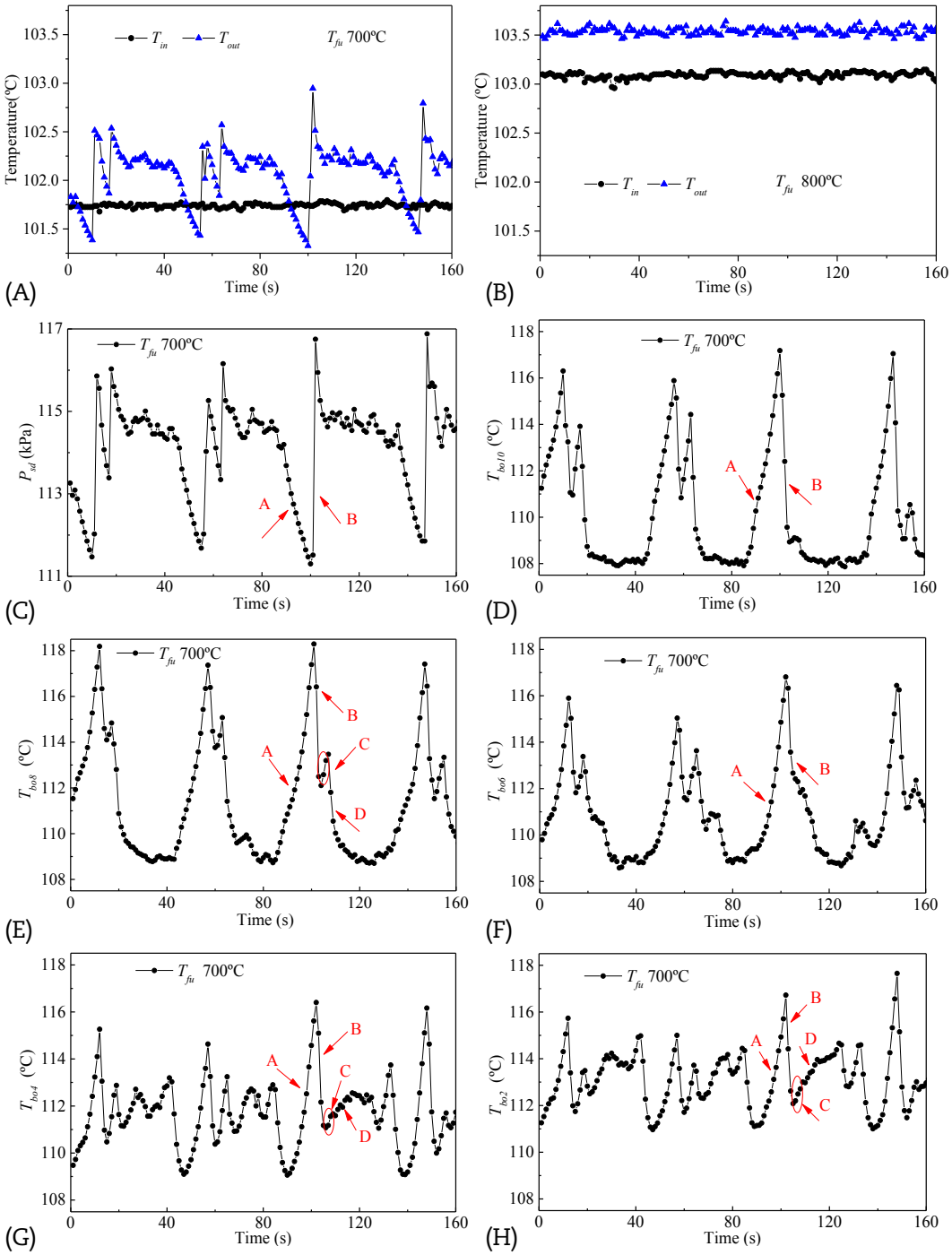


**Fig. 9.** Variation of pressure and temperature with time. (A, B) Temperature variation at the inlet and outlet of the cooling thimble. (C) Pressure change of the steam dome. (D) Temperature change of $T_{bo10}$. (E) Temperature change of $T_{bo8}$. (F) Temperature change of $T_{bo6}$. (G) Temperature change of $T_{bo4}$. (H) Temperature change of $T_{bo2}$. $P_{sd}$, steam dome pressure; $T_{in}$, inlet tempearture; $T_{out}$, outlet temperature; $T_{bo}$, outer wall temperature of bayonet; $T_{fu}$, furnace temperature.

certain point it drops quickly. At the same time, $P_{sd}$ decreases with time slowly at first and then rises sharply; these tendencies are shown separately in stage A and stage B. Arrow C indicates the stage at which the values of $T_{bo2}$, $T_{bo4}$, $T_{bo6}$, $T_{bo8}$, and $T_{bo10}$ rise for a few seconds. However, not all thermocouple measurements have the same variation tendency at stage C. Arrow D corresponds to the stage that shows values of $T_{bo6}$, $T_{bo8}$, and $T_{bo10}$ decreasing with time whereas $T_{bo4}$ and $T_{bo2}$ increase with time. Then, $T_{bo2}$ and $T_{bo4}$ drop quickly, whereas $T_{bo6}$, $T_{bo8}$, and $T_{bo10}$ rise gradually. Finally, the system goes into the next circulation.

Stage A is the initial period of flashing flow instability, in which the water temperature in the rising zone does not reach the local saturation water temperature, resulting in no flashing phenomenon. The system is in a state of single-phase natural circulation. There is only a small amount of vapor being generated from the heating section. In the condenser, this vapor is condensed into water, which can be seen in the glass tube below the condenser. The small amount of vapor has two results. First, the natural circulation driving force is not large enough, causing the main stream to slow down. The slower main stream cannot efficiently remove the heat

from the electric furnace, resulting in the gradual increase in wall temperature. Second, $P_{sd}$ cannot maintain its original value, but decreases gradually during this process.

The occurrence of stage B depends on both temperature and pressure. Because of the slow velocity, the main stream sufficiently absorbs the heat brought in by the furnace, resulting in a small rise in the main stream temperature. Additionally, $P_{sd}$ decreases continually during stage A. When the local saturation water temperature decreases continually, because of decreasing $P_{sd}$, the water will evaporate and flashing will occur. Flashing generates a significant amount of vapor in a short period, which causes $P_{sd}$ to increase sharply. Moreover, the quick growth of vapor increases the natural circulation driving force, which accelerates the flow rate of the main stream. The rapid flow of the main stream observably enhances the flow boiling heat transfer efficiency, resulting in a sharp decrease in wall temperature.

As shown in Fig. 9, the flashing phenomenon of stage C does not appear in every flashing period. This is because the water temperature does not match the local saturation water temperature corresponding to the local pressure. The sharp increase of $P_{sd}$ at stage C makes the water temperature lower than the local saturation water temperature, resulting in a sudden disappearance of flashing [28]. Without the large driving force, the main stream returns to a low velocity and $P_{sd}$ decreases for several seconds. The flashing will occur again when the water temperature reaches the local saturation water temperature. This describes the formation process of stage D. However, at stage D, the behavior of $T_{bo2}$ and $T_{bo4}$ is different from that of $T_{bo6}$, $T_{bo8}$, and $T_{bo10}$.

$T_{bo2}$ and $T_{bo4}$ increase continually, which is the opposite variation tendency of $T_{bo6}$, $T_{bo8}$, and $T_{bo10}$. This is because of the subcooled boiling that occurs at $T_{bo2}$ and $T_{bo4}$. Even though the main stream has a higher velocity during the flashing process, it still cannot remove enough heat because of the small amount of vapor generated from subcooled boiling. Therefore, $T_{bo2}$ and $T_{bo4}$ continually increase. When the wall superheats to some degree, the high heat flux resulting from the high superheat will turn the subcooled boiling into saturation boiling, which will remove more heat. Then, $T_{bo2}$ and $T_{bo4}$ decrease, and the next circulation begins.

In this experimental natural circulation loop with a thimble-type heat transfer element, the flashing instability phenomenon was observed at furnace temperatures of 700°C or less. A furnace temperature of 700°C corresponds to a thimble outer wall temperature of approximately 600°C. The liquidus temperature of molten salt fuel LiF–$BeF_2$–$ThF_4$–$UF_4$ (73–16–10.6–0.3 mol%) used by ORNL is approximately 500°C [29]. After the reactor shuts down, the molten salt fuel is drained into the drain salt tank. When the temperature of the molten salt fuel in the drain salt tank decreases to about 600°C, the flashing instability phenomenon will occur, which can decrease the natural circulation capacity of the cooling thimble and hinder the residual heat removal from the molten salt. As such, the flashing instability should be thoroughly considered to guarantee reactor safety.

### 4.3. Influence of the gas gap width of the cooling thimble on heat transfer rate

#### 4.3.1. Temperature distribution in the thimble tube

The cooling thimble is heated by a high-temperature electric furnace. With proportion integration differentiation (PID) technology, the furnace temperature in each segment can be adjusted automatically, and the temperature can be controlled within 2°C. The furnace temperatures are set at 800°C, 750°C, 700°C, 650°C, 600°C, and 550°C. The axis thermocouple distribution on the thimble tube is shown in Fig. 3. Fig. 10 shows the average values of $T_{to2}$, $T_{to4}$, and $T_{to6}$ at approximately 5 minutes, when the furnace temperature is stable. $L_{hs}$ is the heating section length of the thimble and $L$ is the distance of the thermocouples from the thimble bottom. The points of each shape correspond to a furnace temperature $T_{fu}$. As shown in Fig. 10, the furnace temperature is higher than the outer wall temperature by approximately 100°C, which demonstrates that there is a large temperature difference in the radial direction of the furnace chamber.

#### 4.3.2. Change in heat transfer rate for different gas gap widths and different temperatures

In this section, two methods are used to calculate the heat transfer rate $\Phi$. The first method is to calculate $\Phi_{co}$ and $\Phi_{ra}$ between the bayonet and thimble. The total heat transfer rate obtained from the first method is simplified as $\Phi_{total,1}$. $T_{bo}$ and $T_{ti}$ are used as the boundary conditions to calculate $\Phi_{total,1}$. In the second method, the total heat transfer rate $\Phi_{total,2}$ is calculated using the latent heat of vaporization. Because heat is sufficiently preserved in the experimental loop, the heat loss through the pipeline is neglected and the heat brought in by the furnace is considered to be equal to the heat removed by the vaporization of saturated water. The vapor flow rate can be obtained from the condensed water. The detailed method is illustrated in the section on the experimental facility.

In the calculation process, the outer wall of the thimble is divided into five parts. The temperatures of each part are considered to be uniform and are measured by the thermocouples in each part. The equations used to calculate $\Phi_{total,1}$ and $\Phi_{total,2}$ are Eqs. (12–15). In the equations, $\tau$ is the time of steam condensation and $L_{cw}$ is the height of the condensed water.

$$\Phi_{ra} = \frac{\sigma_1\left(T_{ti}^4 - T_{bo}^4\right)}{A_{bo}(1-\varepsilon_{bo})/\varepsilon_{bo} + 1/A_{bo}X_{bo,ti} + A_{ti}(1-\varepsilon_{ti})/\varepsilon_{ti}} \tag{12}$$

$$\Phi_{co} = \frac{2k\pi L_{hs}(T_{ti} - T_{bo})}{\ln(d_{ti}/d_{bo})} \tag{13}$$

$$\Phi_{total,1} = \Phi_{ra} + \Phi_{co} \tag{14}$$

$$\Phi_{total,2} = \frac{\pi D_{cw}^2 L_{cw} \cdot \left(H''_{sat} - H'_{sat}\right)}{4\tau \cdot v'} \tag{15}$$

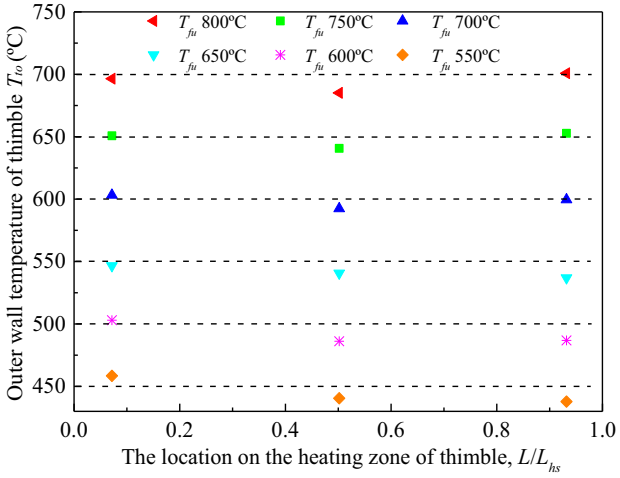


**Fig. 10.** Distribution of outer wall temperature at the corresponding furnace temperature. $T_{to}$, thimble outer wall temperature; $T_{fu}$, furnace temperature; $L_{hs}$, length of the total thimble heating zone; $L$, length from the bottom of thimble heating zone.

To calculate $\Phi_{ra}$ and $\Phi_{co}$, the angle factor $X_{bo,ti}$ is considered to be equal to 1 because the bayonet is surrounded by the thimble. Owing to the large influence of pipe wall emissivity on the radiation heat transfer, the emissivity of the pipe wall was measured by Automatic Detection at the Process Control Systems Research Institute, Harbin Institute of Technology. The results show that $T_{bo}$ is fairly stable, and the average emissivity $\varepsilon_{bo}$ of the bayonet outer wall for different wavelengths is 0.25. However, $T_{ti}$ changes dramatically, and the change in emissivity with temperature can be represented as $\varepsilon_{ti} = 0.0005 \times T - 0.1$. The changes in heat transfer rate with $\overline{T}_{to}$ at different gas gap widths are shown in Fig. 11.

Figs. 11A–11C indicate that there is little difference between the two methods of obtaining the heat transfer rate. The average difference between them is approximately 5%, and the largest difference is within 10%, which demonstrates that the parameter measurement and calculation are relatively accurate. Moreover, as shown in Fig. 11A, the conduction heat transfer rate occupies a relatively larger proportion (more than 75%) of the total heat transfer rate when the gas gap width is 2.0 mm. In contrast, the radiation heat transfer rate occupies a relatively larger proportion (approximately 60%) of the total heat transfer rate when the gas gap width is 8.31 mm. The reason for this is that when the gas gap width is narrow, the heat resistance is small, and the conduction heat transfer rate is very large. Increasing the gas gap width results in an increase of heat resistance and a decrease of conduction heat transfer rate. At the same time, an increase in the radiation heat transfer area results in an increase in the radiation heat transfer rate.

As shown in Fig. 11D, the heat transfer rate at different temperatures decreases when the gas gap width increases. The heat transfer rate at a gas gap width of 2.0 mm is observably larger than that at the 5.05 mm and 8.31 mm gas gap widths. This occurs because the gas gap width is very narrow and the air heat resistance is very small, which makes the conduction heat transfer rate very large. The decrease in the gas gap width will also reduce the radiation heat transfer area, which reduces the radiation heat transfer rate. However, on the whole, the influence of gas gap width on conduction heat transfer rate is larger than the influence of gas gap width on radiation heat transfer rate, resulting in a decrease of the total heat transfer rate as the gas gap width increases. Moreover, Fig. 11D shows that there is little difference in the heat transfer rate between gas gap widths of 5.05 mm and 8.31 mm, where an average difference of results between the two gas gap widths is only 10%. As shown in Figs. 10B and 10C, the conduction heat transfer rate occupies a larger proportion at the 5.05 mm gas gap width, but the radiation heat transfer rate occupies a larger proportion at the 8.31 mm gas gap width. On the whole, there is little difference in the total heat transfer rate between the two widths.

#### 4.3.3. *Calculating the influence of gas gap width on heat transfer rate*

The electric furnace provides high temperature circumstances by electric heating, and transfers heat to the cooling thimble through radiation and conduction heat transfer. This type of structure introduces a problem in that the outer wall temperature of the thimble does not remain constant as the thimble diameter changes. This is because the temperature of the electric furnace interior is nonuniform; the temperature close to the electric furnace wall is higher. In an actual MSR, the outer wall temperature of the thimble changes with the temperature of the molten salt rather than changing with

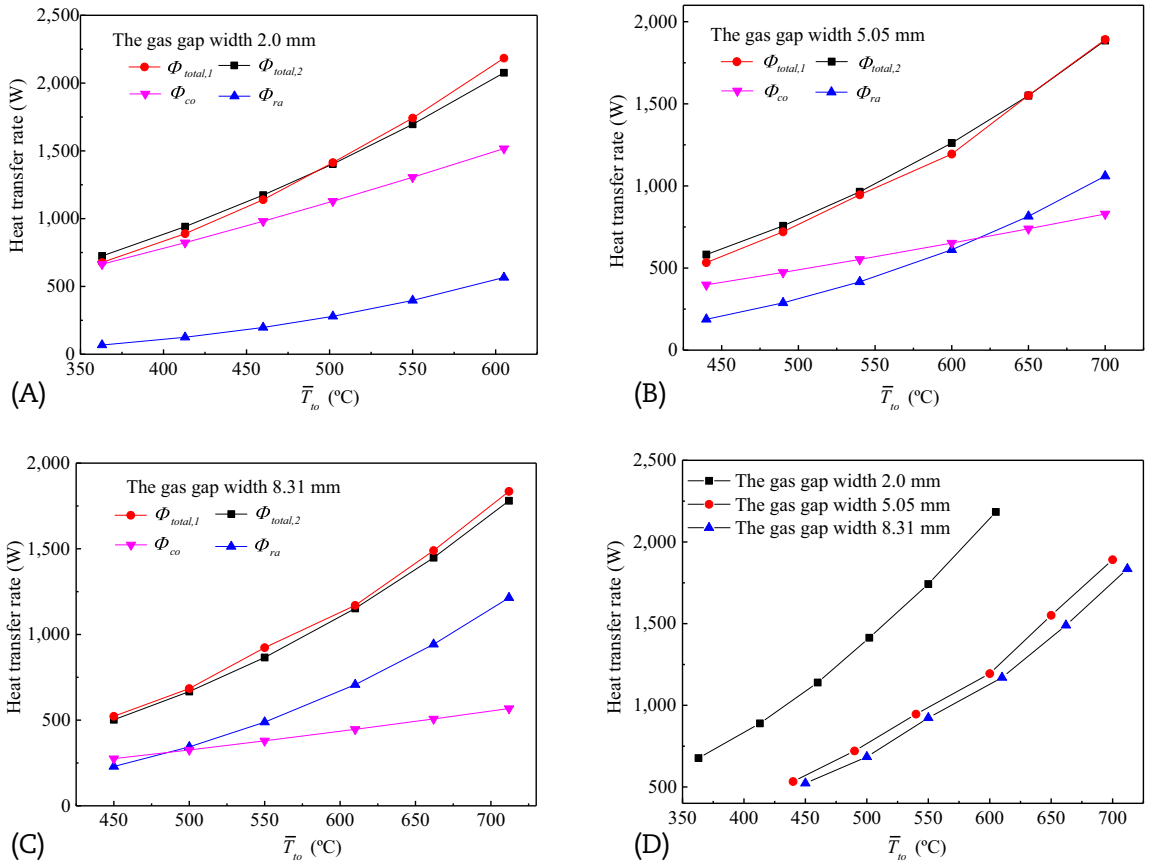


**Fig. 11.** Change in heat transfer rate with temperature at different gas gap widths. $T_{to}$, thimble outer wall temperature; $\Phi_{total,1}$, total heat transfer rate of the first method; $\Phi_{total,2}$, total heat transfer rate of the second method; $\Phi_{co}$, conduction heat transfer rate; $\Phi_{ra}$, radiation heat transfer rate.

the outer wall diameter. Therefore, this experiment does not exactly replicate an actual MSR. In this section, for the calculation, the outer wall temperature of the thimble is assumed to be 700°C, a value which does not vary with thimble diameter. This assumption will allow a better approximation of an actual MSR.

According to the experimental results, the outer wall temperature of the thimble is approximately 700°C when the furnace temperature is 800°C. In this situation, there is no flashing instability phenomenon; the system pressure and wall temperature are both stable. The two-phase flow pressure drop is calculated based on the homogeneous flow model. To calculate the heat transfer rate more accurately, the heating section of the bayonet is divided into five parts. The temperature of each part is considered to be uniform. Considering that heating above $T_{bo4}$ represents saturated boiling and heating below $T_{bo4}$ represents subcooled boiling, different forms of the Chen formulae are applied. Moreover, in the calculation process, the equivalent diameter of the rising channel is larger than 6.0 mm; this channel is considered to be a conventional channel by Mehendale et al. [30] and Kandlikar [31].

This section analyzes the influence of gas gap width on the heat transfer rate using a self-compiling program. The calculation results are shown in Fig. 12.

As shown in Fig. 12A, when the diameter of the thimble is kept at 38 mm and the diameter of the bayonet is changed, the radiation heat transfer rate and the conduction heat transfer rate will decrease together with the increase in gas gap width. It can be concluded that the change in conduction heat transfer rate caused by the change in the gas gap width is more significant than the change in the radiation heat transfer rate caused by the change in the heat transfer area. The change of total heat transfer rate has the same tendency as the change of conduction heat transfer rate.

As shown in Fig. 12B, when the diameter of the bayonet is kept at 25.6 mm and the diameter of the thimble is changed, increasing the gas gap width increases the radiation heat transfer area, causing the radiation heat transfer rate to increase. The variation tendency of the radiation heat transfer rate is slightly different than that shown in Fig. 12A. At the same time, another result of increasing the gas gap width is that the increase will increase the thermal resistance, which will result in a decrease in the conduction heat transfer rate. The total heat transfer rate has the same variation tendency as that of the conduction heat transfer rate. Moreover, when the gas gap width is very narrow, the heat transfer rate decreases sharply with the increase in the gas gap width. The reason for this is that the increase in the gas gap width results in a sharp increase in thermal resistance when the gas gap width is narrow, which makes the conduction heat transfer rate decrease noticeably.

It can be seen in Fig. 12 that the calculation results correspond closely with the experimental results, except that the experimental results are slightly higher than the calculation results for a gas gap width of 8.31 mm. This occurs because there is a temperature gradient in the radial direction of the furnace. The actual values of $\overline{T}_{to}$ are approximately 700°C and 712°C when the gas gap widths are 5.05 mm and 8.31 mm, respectively. However, Fig. 12 is obtained based on the assumption that $\overline{T}_{to}$ is 700°C, because we cannot make the assumption that $\overline{T}_{to}$ is 700°C and 712°C simultaneously in the calculation program. Even so, we can still conclude that the calculation results correspond well with the experimental results shown in the figure.

It can be seen from the calculation results above that the gas gap width has a large influence on the heat transfer rate. With the increase in the gas gap width from 1.0 mm to 11.0 mm, the heat transfer rate decreases from 5.2 kW to 1.6 kW. This conclusion is different from the conclusion drawn by Sun et al. [32], who found that the gas gap width in the bayonet of cooling thimble has little effect on the heat transfer rate. In theory, we can attempt to decrease the gas gap width in order to increase the heat transfer rate. However, when the gas gap width is very narrow, it is very difficult to arrange the thermocouples on the pipe wall. This long, thin structure makes it very difficult to insert the bayonet into the thimble and ensure that the bayonet is exactly in the center of the thimble. Moreover, it would be very expensive to manufacture and install such elaborate cooling thimbles. There is no need to make the gas gap width very thin; we can simply increase the number of cooling thimbles in the actual MSRs to increase the heat removal capacity.

### 4.4. Uncertainty analysis

There are two kinds of uncertainty in this theory. The first category of uncertainty is concerned with repeated parameter measurements, which are generally obtained through statistical analysis. The second category of uncertainty is concerned with systemic error of measuring instruments or environmental and human-introduced error. There is no first category uncertainty in the measurement process of the heat transfer rate, because the parameters were all measured with a single measurement. The uncertainties in the relevant parameters can be calculated based on the Kline–McClintock method [33].

In this experiment, the heat transfer rate of the cooling thimble is measured by Eq. (15), and there is some systemic error introduced by measuring instruments such as thermocouples and pressure transmitters. The thermocouples are calibrated to have an accuracy of 0.5°C; the accuracy of the pressure transmitters is given

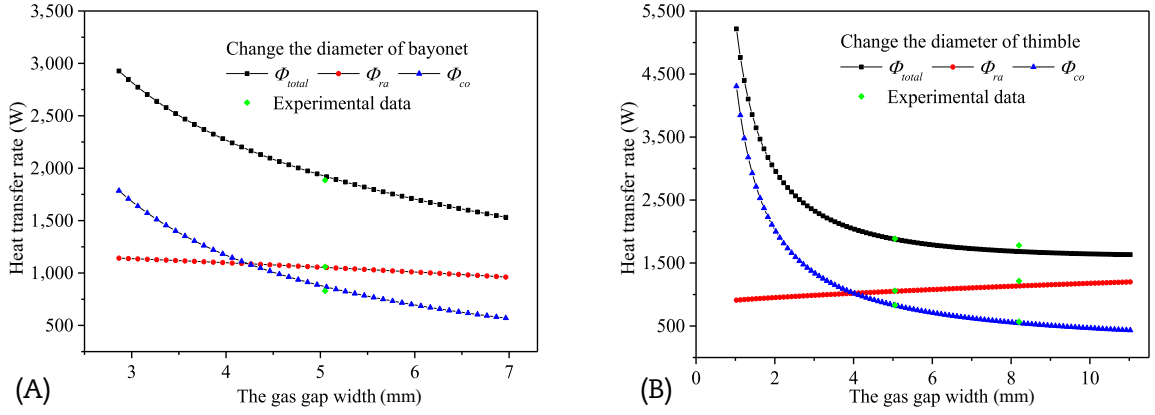


**Fig. 12.** Influence of the gas gap width on the heat transfer rate. Total heat transfer rate ($\Phi_{total}$), Conduction heat transfer rate ($\Phi_{co}$), Radiation heat transfer rate ($\Phi_{ra}$).

by the manufacturer with calibration certificates and is confirmed to be 0.1%. There are also some human-introduced errors in the measuring process. The measurement accuracy of the condensed water height is 0.5 mm; the accuracy of recording time $\tau$ using a stopwatch is 0.5 s.

$$\begin{cases} \dfrac{\partial \ln \Phi}{\partial D_{cw}} = \dfrac{2}{D_{cw}} \\ \dfrac{\partial \ln \Phi}{\partial L_{cw}} = \dfrac{1}{L_{cw}} \\ \dfrac{\partial \ln \Phi}{\partial T} = \dfrac{\partial \ln\left(H''_{sat} - H'_{sat}\right)}{\partial T} = \dfrac{1}{H''_{sat} - H'_{sat}}\left(\dfrac{\partial H''_{sat}}{\partial T} - \dfrac{\partial H'_{sat}}{\partial T}\right) = \dfrac{1}{H''_{sat} - H'_{sat}}\left(\dfrac{H''_{sat,1} - H''_{sat,2}}{T''_1 - T''_2} - \dfrac{H'_{sat,1} - H'_{sat,2}}{T'_1 - T'_2}\right) \\ \dfrac{\partial \ln \Phi}{\partial \tau} = -\dfrac{1}{\tau} \\ \dfrac{\partial \ln \Phi}{\partial v'} = -\dfrac{1}{v'} \cdot \dfrac{\partial v'}{\partial T} = -\dfrac{1}{v'} \cdot \dfrac{v'_1 - v'_2}{T'_1 - T'_2} \end{cases} \tag{16}$$

$$\begin{aligned} \frac{\Delta \Phi}{\Phi} &= \sqrt{\left(\frac{\partial \ln \Phi}{\partial D_{cw}}\right)^2 \cdot \delta D_{cw}^2 + \left(\frac{\partial \ln \Phi}{\partial L_{cw}}\right)^2 \cdot \delta L_{cw}^2 + \left(\frac{\partial \ln \Phi}{\partial T}\right)^2 \cdot \delta T^2 + \left(\frac{\partial \ln \Phi}{\partial \tau}\right)^2 \cdot \delta \tau^2 + \left(\frac{\partial \ln \Phi}{\partial v'}\right)^2 \cdot (\delta v')^2} \\ &= \sqrt{4 \cdot \left(\frac{\delta D_{cw}}{D_{cw}}\right)^2 + \left(\frac{\delta L_{cw}}{L_{cw}}\right)^2 + \left[\left(\frac{H''_{sat,1} - H''_{sat,2}}{T''_1 - T''_2} - \frac{H'_{sat,1} - H'_{sat,2}}{T'_1 - T'_2}\right) \cdot \frac{\delta T}{H'' - H'}\right]^2 + \left(\frac{\delta \tau}{\tau}\right)^2 + \left(\frac{\delta t}{v'} \cdot \frac{v'_1 - v'_2}{T'_1 - T'_2}\right)^2} \end{aligned} \tag{17}$$

Taking the measuring time and condensed water height into consideration, the uncertainty in the heat transfer rate can be calculated using Eqs. (16) and (17). Bringing the values into the equation, the uncertainty in the heat transfer rate is found to be 0.39%.

## 5. Conclusion

1. Noncondensed air in the system will increase the system pressure considerably, so it should be drained out of the system before the experiment startup process. The noncondensed air will significantly decrease the condensation heat transfer efficiency.
2. In a flashing situation, the water temperature is higher than the local saturation water temperature. Superheat of the water will cause the water to evaporate. The generated vapor will then drop the hydrostatic head to a lower position. Because of this, the flashing start point moves downward rapidly, which accelerates the main stream. The flashing disappears when the water temperature is lower than the local saturation water temperature. When the energy accumulates to a certain degree, flashing will occur again. Subcooled boiling has also been found underneath the heat transfer element. The flashing flow instability should be considered in an actual drain salt tank of an MSR to ensure that the residual heat of molten salt can be reliably removed.
3. There is little difference between the two methods of obtaining the heat transfer rate, with an average difference of approximately 5%. At the same thimble outer wall temperature, the heat transfer rate at a gas gap width of 5.05 mm is similar to the heat transfer rate at a gas gap width of 8.31 mm, with an average relative error of approximately 10%. However, the heat transfer rate at a gas gap width of 2.0 mm is much larger; the heat transfer rate increases by 95% when the gas gap width decreases from 5.05 mm to 2.0 mm, which demonstrates that the heat transfer rate can decrease significantly with an increase in gas gap width when the gas gap width is narrow. However, the heat transfer rate hardly changes when the gas gap width increases to a certain degree.
4. The calculation results indicate that the gas gap width has a large influence on the heat transfer rate. With the increase in the gas gap width from 1.0 mm to 11.0 mm, the heat transfer rate decreases by 70%, from 5.2 kW to 1.6 kW. The conduction heat transfer rate decreases by 90%, from 4.3 kW to 0.432 kW, and the radiation heat transfer rate increases by 32%, from 0.91 kW to 1.2 kW. This indicates that the influence of changing the gas gap width on the conduction heat transfer rate is much larger than that on the radiation heat transfer rate. We can in theory attempt to decrease the gas gap width in order to increase the heat transfer rate, but we should also take the fabrication difficulty and economics into consideration.

## Conflicts of interest

The authors have no conflict of interest.

## Acknowledgments

This work is conducted with financial support of National Natural Science Foundation of China (Grant No. 11475048) and support of National Natural Science Foundation of China (Grant No. 11605032).

## Nomenclature

| | |
|---|---|
| $A$ | area ($m^2$) |
| $C_p$ | specific heat at constant pressure (kJ/(kg K)) |
| D | equivalent diameter (m) |
| $F$ | enhancement factor |
| $fr$ | friction factor |
| $G$ | mass flux (kg/(m2 s)) |

| | |
|---|---|
| $h$ | heat transfer coefficient (W/(m2 K)) |
| $H$ | enthalpy (W) |
| $K$ | thermal conductivity (W/(m K)) |
| P | pressure (Pa) |
| $Pr$ | Prandtl number |
| $Re$ | Reynolds number |
| $S$ | suppression factor |
| $T$ | temperature (K) |
| $x$ | dryness fraction |
| $X$ | angle factor |
| $X_{tt}$ | Martinelli parameter |

*Greek symbols*

| | |
|---|---|
| $\Delta P$ | pressure drop (Pa) |
| $\Delta T_{sat}$ | inner wall superheat of thimble, $T_{bi}$-$T_{sat}$ (K) |
| $\varepsilon$ | emissivity of pipe wall |
| $\mu$ | dynamic viscosity (Pa·s) |
| $\upsilon$ | specific volume (m3/kg) |
| $\sigma$ | surface tension coefficient (N/m) |
| $\sigma_1$ | Stefan-Boltzmann constant |
| $\tau$ | record time (s) |
| $\Phi$ | heat transfer rate (W) |

*Subscripts*

| | |
|---|---|
| *a* | acceleration resistance |
| *ba* | bayonet |
| *bi* | bayonet inner wall |
| *bo* | bayonet outer wall |
| *co* | conduction |
| *cw* | condensed water |
| *f* | friction resistance |
| *fi* | feed tube inner wall |
| *fo* | feed tube outer wall |
| *fu* | furnace |
| *g* | gravity resistance |
| *hs* | heat section |
| *pool* | pool boiling |
| *ra* | radiation |
| *rc* | rising channel |
| *ti* | thimble inner wall |
| *to* | thimble outer wall |
| *tp* | two phase |
| *sat* | saturation |
| *sd* | steam dome |

*Superscripts*

| | |
|---|---|
| $'$ | liquid phase |
| $''$ | gas phase |

## References


[1] D.E. Holcomb, S.M. Cetiner, An Overview of Liquid–fluoride–salt Heat Transport Systems, ORNL Report no. ORNL/TM-2010/156, ORNL, Oak Ridge, TN, 2010.

[2] R.C. Robertson, MSRE design and Operations Report: Part I. Description of Reactor Design, Oak Ridge National Laboratory Reports, 1965.

[3] P.N. Haubenreich, J.R. Engel, B.E. Prince, H.C. Claiborne, MSRE design and Operations Report: Part III. Nuclear Analysis, Technical Report ORNL-TM-730, ORNL, Oak Ridge, TN, 1964.

[4] R. Tallackson, MSRE Design and Operations Report: Part IIA. Nuclear and Process Instrumentation, ORNL-TM-729, 1968.

[5] D.E. Holcomb, G.F. Flanagan, G.T. Mays, W.D. Pointer, K.R. Robb, G.L. Yoder Jr., Fluoride Salt-cooled High-temperature Reactor Technology Development and Demonstration Roadmap, Office of Scientific and Technical Information Technical Reports, 2013.

[6] T. Ishiguro, W.F.G. van Rooijen, Y. Shimazu, H. Mochizuki, Design of a passive residual heat removal system for the FUJI-233Um molten salt reactor system, Ann. Nucl. Energy 64 (2014) 398–407.

[7] V. Ignatiev, O. Feynberg, I. Gnidoi, A. Merzlyakov, V. Smirnov, A. Surenkov, I. Tretiakov, R. Zakirov, V. Afonichkin, A. Bovet, V. Subbotin, A. Panov, A. Toropov, A. Zherebtsov, Progress in development of Li, Be, Na/F Molten Salt Actinide Recycler and Transmuter Concept, Proceedings of the ICAPP, 2007. Nice, France.

[8] E. Merle-Lucotte, D. Heuer, M. Allibert, M. Brovchenko, N. Capellan, V. Ghetta, Launching the thorium fuel cycle with the molten salt fast reactor, in: International Congress on Advances in Nuclear Power Plants, 2011.

[9] T. Iwamura, Y. Murao, F. Araya, K. Okumura, A concept and safety characteristics of JAERI passive safety reactor (JPSR), Prog. Nucl. Energy 29 (1995) 397–404.

[10] P.E. Juhn, J. Kupitz, J. Cleveland, B. Cho, R.B. Lyon, IAEA activities on passive safety systems and overview of international development, Nucl. Eng. Des. 201 (2000) 41–59.

[11] Y.P. Zhang, S.Z. Qiu, G.H. Su, W.X. Tian, Analysis of safety margin of in-vessel retention for AP1000, Nucl. Eng. Des. 240 (2010) 2023–2033.

[12] C. Wang, Z. Guo, D. Zhang, S. Qiu, W. Tian, Y. Wu, G. Su, Transient behavior of the sodium–potassium alloy heat pipe in passive residual heat removal system of molten salt reactor, Prog. Nucl. Energy 68 (2013) 142–152.

[13] J.A. Boure, A.E. Bergles, L.S. Tong, Review of two-phase flow instability, Nucl. Eng. Des. 25 (1973) 165–192.

[14] S. Kakac, B. Bon, A review of two-phase flow dynamic instabilities in tube boiling systems, Int. J. Heat Mass Transfer 51 (2008) 399–433.

[15] G.D. Prasad, M. Pandey, M.S. Kalra, Review of research on flow instabilities in natural circulation boiling systems, Prog. Nucl. Energy 49 (2007) 429–451.

[16] S.Y. Jiang, X.X. Wu, Y.J. Zhang, Experimental study of two-phase flow oscillation in natural circulation, Nucl. Sci. Eng. 135 (2000) 177–189.

[17] S.Y. Jiang, M.S. Yao, J.H. Bo, S.R. Wu, Experimental simulation study on start-up of the 5 MW nuclear heating reactor, Nucl. Eng. Des. 158 (1995) 111–123.

[18] M. Furuya, F. Inada, T.H.J.J. van der Hagen, Flashing-induced density wave oscillations in a natural circulation BWR—mechanism of instability and stability map, Nucl. Eng. Des. 235 (2005) 1557–1569.

[19] K. Tanimoto, M. Ishii, S.Y. Lee, Examination of transient characteristics of two-phase natural circulation within a Freon-113 boiling/condensation loop, Nucl. Eng. Des. 183 (1998) 77–95.

[20] S. Shi, T. Hibiki, M. Ishii, Startup instability in natural circulation driven nuclear reactors, Prog. Nucl. Energy 90 (2016) 140–150.

[21] J. Chen, S. Yang, S. Liao, X. Cao, Experimental investigation of effective parameters on geyser periodicity in a vertical heated system, Exp. Thermal Fluid Sci. 68 (2015) 163–176.

[22] L.L. Tong, G. Shao, K. Yuan, X.W. Cao, An experimental study on geysering phenomena induced by buoyancy in a heating system, Ann. Nucl. Energy 63 (2014) 129–137.

[23] R.N. Duffey, U.S. Rohatgi, Physical interpretation of geysering phenomena and periodic boiling instability at low flows, in: ASME/JSME International Conference on Nuclear Engineering, New Orleans, LA, 1996.

[24] O.R.N. Laboratory, Molten-Salt Reactor Program Semiannual Progress Report, July 31, 1963.

[25] J.C. Chen, Correlation for boiling heat transfer to saturated fluids in convective flow, Ind. Eng. Chem. Process. Des. 5 (1966) 322–329.

[26] J. Yan, Q. Bi, Z. Liu, G. Zhu, L. Cai, Subcooled flow boiling heat transfer of water in a circular tube under high heat fluxes and high mass fluxes, Fusion Eng. Des. 100 (2015) 406–418.

[27] L. Wu, Y. Liu, H. Jia, J. Wang, Innovative flow-resistance performance in the single-phase natural circulation loop and relevant experiment verification, Int. J. Heat Mass Transfer 107 (2017) 66–73.

[28] X. Hou, Z. Sun, J. Su, G. Fan, An investigation on flashing instability induced water hammer in an open natural circulation system, Prog. Nucl. Energy 93 (2016) 418–430.

[29] S. Cantor, J.W. Cooke, A.S. Dworkin, G.B. Robbins, R.E. Thoma, G.M. Watson, Physical Properties of Molten-salt Reactor Fuel, Coolant and Flush Salts, ORNL-TM-2316, Oak Ridge National Laboratory, 1968.

[30] S.S. Mehendale, A.M. Jacobi, R.K. Shah, Fluid flow and heat transfer at micro and meso-scales with application to heat exchanger design, Appl. Mech. Rev. 53 (2000) 175–193.

[31] S.G. Kandlikar, Fundamental issues related to flow boiling in minichannels and microchannels, Exp. Thermal Fluid Sci. 26 (2002) 389–407.

[32] L. Sun, L. Sun, C. Yan, D. Fa, Conceptual design and analysis of a passive residual heat removal system for a 10MW molten salt reactor experiment, Prog. Nucl. Energy 70 (2014) 149–158.

[33] S.J. Kline, F.A. McClintock, Describing uncertainties in single-sample experiments, Mech. Eng. 75 (1953) 3–8.